Inorganic Chemistry
Article
Cite This: Inorg. Chem. 2018, 57, 11382−11392
pubs.acs.org/IC

Chalcogen Impact on Covalency within Molecular $[Cu_3(\mu_3\text{-E})]^{3+}$ Clusters (E = O, S, Se): A Synthetic, Spectroscopic, and Computational Study

Brian J. Cook,[†,‡] Gianna N. Di Francesco,[†,‡] Ricardo B. Ferreira,[†,‡] James T. Lukens,[§] Katharine E. Silberstein,[§] Brenna C. Keegan,[⊥] Vincent J. Catalano,[⊥] Kyle M. Lancaster,*[,§] Jason Shearer,*[,⊥,△] and Leslie J. Murray*[,†]

[†]Center for Catalysis and Florida Center for Heterocyclic Compounds, Department of Chemistry, University of Florida, Gainesville, Florida 32611-7200, United States

[§]Department of Chemistry and Chemical Biology, Cornell University, Ithaca, New York 14853, United States

[⊥]Department of Chemistry, University of Nevada, Reno, Reno, Nevada 89557, United States

Supporting Information

ABSTRACT: Reaction of the tricopper(I)−dinitrogen tris(β-diketiminate) cyclophane, $Cu_3(N_2)L$, with O-atom-transfer reagents or elemental Se affords the oxido-bridged tricopper complex $Cu_3(\mu_3\text{-O})L$ (**2**) or the corresponding $Cu_3(\mu_3\text{-Se})L$ (**4**), respectively. For **2** and **4**, incorporation of the bridging chalcogen donor was supported by electrospray ionization mass spectrometry and K-edge X-ray absorption spectroscopy (XAS) data. Cu $L_{2,3}$-edge X-ray absorption data quantify 49.5% Cu 3d character in the lowest unoccupied molecular orbital of **2**, with Cu 3d participation decreasing to 33.0% in **4** and 40.8% in the related sulfide cluster $Cu_3(\mu_3\text{-S})L$ (**3**). Multiedge XAS and UV/visible/near-IR spectra are employed to benchmark density functional theory calculations, which describe the copper−chalcogen interactions as highly covalent across the series of $[Cu_3(\mu\text{-E})]^{3+}$ clusters. This result highlights that the metal−ligand covalency is not reserved for more formally oxidized metal centers (i.e., $Cu^{III} + O^{2-}$ vs $Cu^{II} + O^{-}$) but rather is a significant contributor even at more typical ligand-field cases (i.e., $Cu_3^{II/II/I} + E^{2-}$). This bonding is reminiscent of that observed in p-block elements rather than in early-transition-metal complexes.

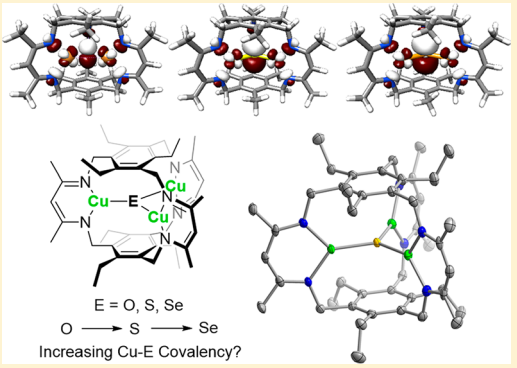

INTRODUCTION

Copper chalcogenides, $Cu_{2-x}E$, have diverse applications, ranging from light harvesting in photovoltaics to sensors and battery materials.[1] The broad utility of the binary, and by extension the related ternary and quaternary, materials arises from the ease of access to substoichiometric compositions (i.e., intermediate between CuE and Cu_2E), which allows for tunable concentrations of charge carriers, provides for site vacancies for accommodating other ions, and can afford electroluminescence and surface plasmon resonance properties.[2] Despite their growing importance, a detailed understanding of the electronic structure of these materials and, consequently, the band structure of the extended solids remains lacking. This deficiency is evident; X-ray photoelectron (XPS) and absorption (XAS) spectroscopy data are inconsistent with the calculated band structures.[3] Model systems that report on the nature of Cu−E interactions, such as the degree of covalency and charge delocalization, are of critical importance to modeling and predicting the properties of this class of materials, including Cu−O zeolites.[4] Molecular copper chalcogenide clusters remain an active area of research, with the aim of interrogating the metal−ligand interactions and developing nanoscale models for the bulk materials.

A notable example of the ambiguities surrounding copper−chalcogen bonding concerns studies on an amine-supported $[Cu_3S_2]^{3+}$ cluster reported by Brown et al.[5] Initially, the oxidation states were assigned as two μ_3-sulfides with formally two Cu^{II} ions and one Cu^{III} ion. In light of the ongoing electronic structure discussions in which descriptors such as oxocopper(III) and oxylcopper(II) are frequently advanced, an alternate formalism would invoke ligand-based oxidation.[4,6] Indeed, more recent work—in particular, by Berry and coworkers[7]—provides strong evidence in support of an alternate electronic structure:[8] a bridging subsulfide or S_2^{3-} couples antiferromagnetically to three Cu^{II} cations. As alluded to above, Cu−O species containing formally high oxidation states (e.g., Cu^{III}) are invoked as reactive intermediates in biological chemistry and catalysis.[6a,e,9] For example, the formal $[Cu^{III}-OH]^{2+}$ moiety has been demonstrated as a potent agent for H•

Received: April 12, 2018
Published: August 30, 2018

DOI: 10.1021/acs.inorgchem.8b01000
Inorg. Chem. 2018, 57, 11382−11392

abstraction.[10] However, a number of core-level spectroscopic studies has called into question the physical accuracy of d^8 Cu^{III} assignments.[11] The origin of this ambiguity is suggested to stem from Cu occupying a position where covalent bonding supplants dative, coordinate metal−ligand interactions; coinage metals sit within a boundary region between the main group and transition elements.[12]

Low-valent multicopper motifs, including $[Cu^{II}_2O]^{2+}$ units, have been identified as the active species in zeolite-based catalysts for methane hydroxylation.[6b,c] Arguments have been advanced that such units owe their reactivity to significant oxyl (suboctet $O^{\bullet-}$) character.[6b−d] Similar electronic structure descriptions have been proposed for trigonal-planar copper(II) and iron(III) iminyl radicals versus the metal imido formalism.[13] Such arguments can themselves naturally follow from the view of Cu−O motifs as highly covalent units; however, detailed studies aimed at validating such notions for these species are rare. The accepted notion of the metal−oxygen covalency is reserved for the highest plausible oxidation states where hole character is invoked for the ligand and has not been suggested for typical oxidation states; that is, $Cu^{III}-O^{2-}$ is ambiguous, whereas $Cu^{II}-O^{2-}$ is not.

One of our groups has reported the synthesis of a sulfide-bridged complex, $Cu_3(\mu_3\text{-S})L$ (**3**), from the reaction of S-atom sources (e.g., S_8 or trimethylphosphine sulfide) with a $Cu^{I}_3-N_2$ complex, **1** (Scheme 1).[14] To advance the discussion of

Scheme 1. Synthesis of 2 and Selenide Congener 4

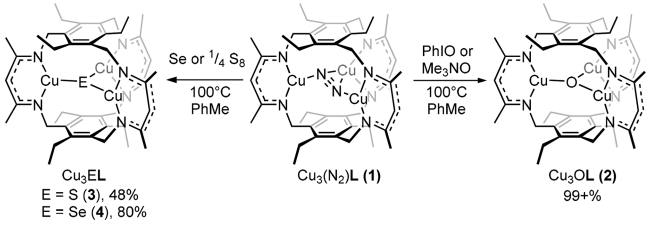

electronic structure−function relationships in Cu−E units, we sought to access the corresponding oxide- and selenide-bridged congeners and use spectroscopic and computational methods to probe the electronic structure of this series of compounds. To our knowledge, there are no prior examples of an isostructural series of $[Cu_3(\mu_3\text{-E})]^{3+}$ clusters. For E = S, parallels can be made to the (μ-sulfido)multicopper compounds from Mankad and Hillhouse as well as the aforementioned $[Cu_3S_2]^{3+}$ cluster.[15] For E = O, $[Cu_3O]^{n+}$ clusters supported by pyrazolates (n = 4, 5) or a macrotetracyclic amine (n = 4) have been synthesized and characterized,[16] although reduction to the 3+ state was not reported. Similarly, the 3+ cluster is unknown in enzymatic systems; the closest comparison is the rapid reduction of the native intermediate in multicopper oxidases, a (μ-hydroxo)(μ_3-oxo)tricopper(II) cluster, to the all-cuprous state.[17] All cupric oxide-bridged clusters are well precedented, including a (μ-oxo)tricopper(II) compound reported by Suh and co-workers,[16c] although the bonding picture in these clusters lacks the ambiguity of the partially oxidized species.

Herein we report the synthesis and characterization of $Cu_3(\mu_3\text{-O})L$ (**2**) and $Cu_3(\mu_3\text{-Se})L$ (**4**), as well as further spectroscopic studies on the previously reported sulfide-bridged compound **3**. Using spectroscopic methods, including Cu K-, Cu $L_{2,3}$-, and S and Se K-edge XAS coupled to electronic structure calculations, we directly compare the effect of the chalcogen on the electronic structure. In particular, we show that the amount of Cu $3d_\pi$ character in the lowest unoccupied molecular orbital (LUMO) diminishes slightly across the series, but, nevertheless, the Cu−E interactions remain covalent and comparable for the O, S, and Se compounds. A consistent electronic structure emerges, showcasing the highly covalent nature of bonding between Cu and all of the chalcogens even in the absence of a formal Cu^{III} center. Owing to the covalent and delocalized nature of the LUMO common to all three species, we ultimately deem the assignment of formal oxidation states to the Cu ions in these tricationic clusters (e.g., $Cu^{I}_2Cu^{II}$ or $Cu^{I}Cu^{II}_2$) to be overly simplistic.

RESULTS AND DISCUSSION

Synthesis of 2 and 4. Using a slightly modified protocol relative to that reported for **3**, reaction of the dinitrogen−tricopper(I) complex, **1**, with metallic Se at 100 °C for 2 h in toluene affords a dark-green solution of **4**, which can be isolated from the reaction mixture in an 86% yield (Scheme 1). Substituting the elemental chalcogen for an O-atom donor in the protocol described above, such as trimethylamine *N*-oxide or iodosobenzene, affords the dark-brown-yellow microcrystalline product **2** in quantitative yield (Scheme 1). Analogous to the sulfide congener, **2** and **4** are diamagnetic and 3-fold-symmetric (D_{3h}) on the NMR (^{1}H and ^{13}C) time scale (Figures S3−S9). For the oxide-bridged compound, we do not observe paramagnetic broadening or shifting in spectra recorded between −85 and +95 °C. High-resolution electrospray ionization mass spectrometry (HR-ESI-MS) spectra on solutions of **2** and **4** agree with the formulations of Cu_3OL and Cu_3SeL, where L^{3-} is the cyclophanate $C_{45}H_{63}N_6^{3-}$. In addition, IR absorption spectra for **2**−**4** are comparable, with no evidence for an E−H vibration, which is consistent with the absence of the corresponding E−H resonance in the NMR spectra recorded in anhydrous and air-free solvents. Taken together, our results are consistent with (μ_3-oxido)- and (μ_3-selenido)tricopper complexes as the products of net chalcogen substitution of N_2 in **1**. As noted above, complex **2** represents a unique example of a $[Cu_3O]^{3+}$ cluster because all reported oxidotricopper complexes contain more oxidized clusters;[16a,b] spectroscopic and theoretical interrogations of its molecular and electronic structures are discussed below.

X-ray diffraction (XRD) data obtained from single crystals grown from the slow evaporation of a saturated benzene solution of **4** reveal a molecular formula of Cu_3SeL (Figure 1). The molecule is isostructural to the S analogue and consistent with the D_{3h} ^{1}H NMR spectrum as well as the molecular formula obtained from HR-ESI-MS. The molecule has near-crystallographic 3-fold symmetry in the solid state, with statistically identical Cu−Se bond lengths [2.1942(4), 2.1944(4), 2.1926(4) Å] and equally similar Cu−N bond lengths [1.908(2)−1.915(3) Å]. Each Cu is trigonal-planar, as in **3**. The N−Cu−N bond angles of 101.9−102.3° are slightly more acute than the corresponding angle in **3**, owing to the larger size of Se versus S. The Cu−Se bond lengths are much shorter than those reported for typical Cu−Se single bonds (2.302−2.524 Å)[18] and could arise from Cu−Se multiple-bonding character or as a consequence of the geometric constraints imposed by the ligand.

Despite multiple attempts to obtain X-ray-quality crystals of **2**, we were able to obtain only microcrystalline powders. Therefore, we utilized Cu K-edge XAS to obtain structural

DOI: 10.1021/acs.inorgchem.8b01000
Inorg. Chem. 2018, 57, 11382−11392

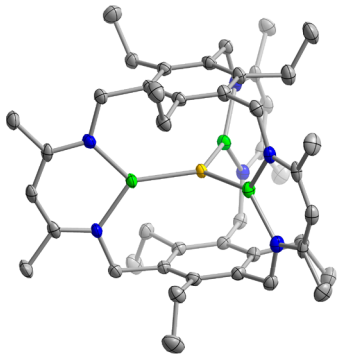

Figure 1. ORTEP representation of **4**. Solvent guests and H atoms have been omitted for clarity. Blue, green, yellow-orange, and gray ellipsoids (70% probability) represent N, Cu, Se, and C atoms, respectively.

information for **2**. The extended X-ray absorption fine structure (EXAFS) region of the Cu K-edge XAS of **2** is best

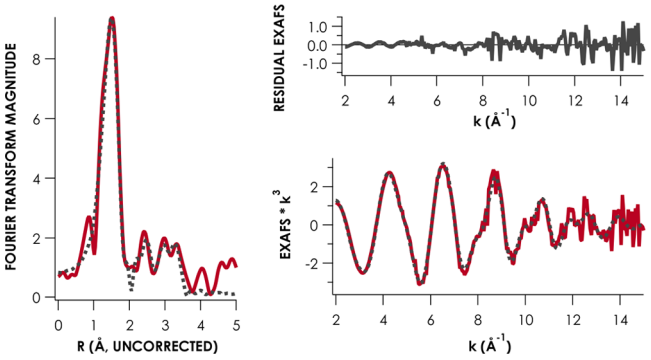

Figure 2. Fourier-transformed k^3-weighted EXAFS (left) and k^3-weighted EXAFS (bottom right) of **2**. The experimental data are given as solid red spectra, and the statistically most significant model is given as dashed black spectra. The top right plot gives the difference between the experimental data and the model for the k^3-weighted EXAFS of **2**. Simulation parameters: shell #1 (Cu−N), n = 2, r = 1.981(3) Å, σ^2 = 0.0045(4) Å^2; shell #2 (Cu−O), n = 1, r = 1.867(4) Å, σ^2 = 0.0034(6) Å^2; shell #3 (Cu−C), n = 2, r = 2.72(3) Å, σ^2 = 0.004(1) Å^2; shell #4 (Cu−C), n = 3, r = 3.449(13) Å, σ^2 = 0.0035(8) Å^2; shell #5 (Cu−C), n = 3, r = 3.95(3) Å, σ^2 = 0.006(2) Å^2; E_0 = 8991.2 eV; ε^2 = 0.61.

fit with two Cu−N scatterers at 1.98 Å and a shorter Cu−O scatterer at 1.87 Å (Figure 2). The separation of the N/O scatterers is warranted by the quality of the data; it is expected that two shells separated by 0.12 Å or more is resolvable for the k-space range over which the data for **2** were analyzed over. Comparable Cu−N bond distances are observed for **1** (viz., 1.8805 and 1.9278 Å) and for (μ_3-sulfido)tricopper cyclophanate (viz., 1.930−1.936 Å; Table 1).[14,20] Cu−C single-scatter pathways found between 2.0 and 3.5 Å in the Fourier-transformed k^3-weighted EXAFS spectrum resulting from scattering by the ligand scaffold could be successfully modeled. This model is thus consistent with the proposed [$Cu_3(\mu_3$-O)]$^{3+}$ core supported by the cyclophane ligand.

Table 1. Bond Metrics for 2−4 Determined from XAS and XRD

	2[a] (Å)	**3**[b] (Å)	**4**[b] (Å)
Cu−N	1.981(3)	1.930(3)	1.910(2)
Cu−Cu	n/a	3.649	3.799
Cu−E (E = O, S, Se)	1.867(4)	2.1069(9)	2.1937(4)

[a]Obtained using Cu K-edge EXAFS. [b]Obtained from XRD.

Cu K-edge X-ray Absorption Near-Edge Structure (XANES) of 2−4. To define the electronic structure of **2** and understand how it is influenced by changes in the central chalcogen ligand, we performed XAS studies combined with electronic structure calculations. The Cu K-edge XANES of **2** (Figure 3) features a weak pre-edge peak at 8978.7(2) eV,

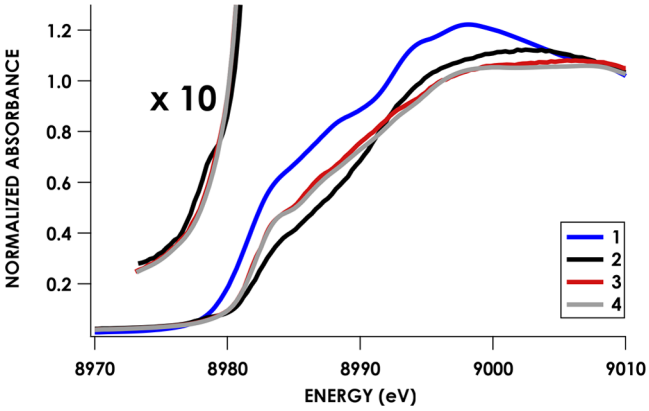

Figure 3. XANES regions of the Cu K-edge XAS spectra of **1**−**4**. Pre-edge regions of the spectra obtained for **2**−**4** are presented as a 10× magnified inset.

corresponding to a formally dipole-forbidden, quadrupole-allowed Cu 1s → 3d excitation. A pronounced shoulder is present at 8985.7(2) eV, which by convention we assign as formally dipole-allowed Cu 1s → 4p + ligand-to-metal charge-transfer (LMCT) shakedown transitions (vide infra).[19] The rising-edge inflection point in the XANES of **2** is at 8986.6(1) eV, which is blue-shifted by 4.1 eV relative to the precursor **1** [8982.5(1) eV]. We have previously communicated that **1** is best described as a closed-shell d^{10} Cu^{I}_3 complex,[20] and the increase in the edge energy exhibited by **2** suggests increased positive charge at the Cu nuclei relative to **1**. This result supports oxidation of the Cu_3 core upon incorporation of the O-atom bridge in **2**.

The Cu K-edge XANES observed for complexes **3** and **4** (Figure 3) are different from that of **2**, but they are strikingly similar to one another. Each lacks a resolved Cu 1s → 3d transition and displays intense shoulders at 8984.4(2) eV, corresponding to Cu 1s → 4p + LMCT shakedown transitions. Furthermore, the rising-edge inflection point for **3** and **4** is slightly red-shifted by 0.5 eV to 8986.1(1) eV. The combination of a red shift in the edge coupled with a substantial decrease in the intensity of the Cu 1s → 3d transition (vide infra) indicates a reduction in the Cu hole character to the low-energy acceptor states. This conclusion is supported by Cu $L_{2,3}$-edge XAS and electronic structure calculations (vide infra).

Cu $L_{2,3}$-Edge XAS on 2−4. The Cu $L_{2,3}$-edge XAS of **2** is displayed in Figure 4. Major peaks are conventionally assigned as Cu 2p → 3d excitations. The $L_{2,3}$ peak energies for **2**−**4** are compiled in Table 2. L_3 peaks of ca. 930.8−931.5 eV, which systematically increase in energy upon going from **2** to **4**, are typical for Cu^{II} species (and ca. 2 eV lower than those of bona fide Cu^{III} species).[21] It should be noted, however, that both

DOI: 10.1021/acs.inorgchem.8b01000
Inorg. Chem. 2018, 57, 11382−11392

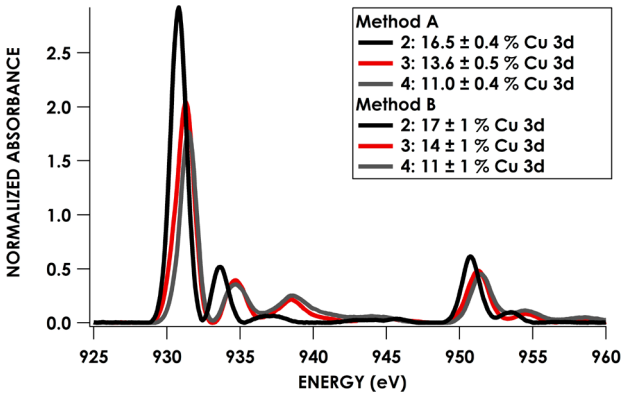

Figure 4. Cu $L_{2,3}$-edge XAS data obtained for **2**–**4**. % Cu 3d contributions to the a_2'' LUMO were determined by a comparison of the total L_2 + L_3 peak areas to that of $(nmph)_2CuCl_4$, for which the Cu 3d contribution to the SOMO is 61%.[23b] Errors in method A were obtained from a least-squares fitting, while those in method B were obtained by applying a 5% error to the total L_3 + L_2 integrated area. The full table of values can be seen in Table S8.

Table 2. Cu $L_{2,3}$-Edge Maxima from Spectra for 2–4

compound	L_3 (eV)	L_2 (eV)	% Cu/hole[a]
2	930.8	950.7	50(1)
3	931.3	951.2	41(1)
4	931.5	951.4	33(1)

[a]Referenced to $(nmph)_2[CuCl_4]$; % Cu 3d/hole = 61%.[23b]

inverted bonding schemes and XAS metal-to-ligand charge-transfer features can complicate comparisons of XAS energies.[11a,22] Using the $L_{2,3}$-edge XAS of D_{4h} $(nmph)_2[CuCl_4]$ [with 61% Cu 3d character in its singly occupied molecular orbital (SOMO)] as a standard,[23] the total integrated area of the L_3 and L_2 peaks in the spectrum of **2** report 16.5(4)% Cu 3d character per hole in the acceptor molecular orbital (MO). Given the three Cu centers, these values amount to a total Cu 3d contribution of 50(1)% per hole. Thus, the $L_{2,3}$-edge XAS reports the absence of 1.06 electrons between the three Cu centers. Progressively more Cu^I character is attained as the chalcogen is varied from O to Se; S-containing **3** possesses 41(1)% Cu character per hole, while Se-containing **4** possesses 31(1)% Cu character per hole.

Ligand K-Edge XAS. Ligand K-edge XAS data were obtained to account for the contribution of the μ_3-chalcogenide donors to the LUMO. S K-edge XAS data obtained for **3** exhibit an intense pre-edge feature at 2472.0 eV assigned by analogy to **2** as S 1s → a_2'' LUMO (Figure 5a). The intensity of this peak (D_0) was used to determine the S 3p contribution to a_2'' (α^2) using eq 1:

$$D_0 = \frac{\alpha^2 I_s h}{3n} \quad (1)$$

where h is the number of holes in the acceptor orbital, n is the number of degenerate photoabsorbers, and I_s is the dipole integral corresponding to a pure S 1s → S 3p absorption. The value of I_s for **3** was estimated at 10.6 based on the assignment of the S 1s → S 4p transition at 2475.3 eV.[24] The corresponding S 3p contribution to a_2'' is 30.2(1)%. Se K-edge XAS data were obtained for **4**. These data show a pre-edge feature at 12651.2 eV, which is poorly resolved from the rising edge (Figure 5b). Although these data indicate covalent bonding between the Cu_3 unit and Se ligand, quantification of the degree of Cu–Se covalency in **4** is precluded owing to the paucity of the Se K-edge data of compounds with well-defined M–Se covalency coupled with the uncertainty in the extracted pre-edge peak area owing to the overlap of the pre-edge peak with the edge itself.

Electrochemical and UV/Visible/Near-IR (NIR) Spectroscopic Studies. The visible absorption spectrum of **4** as a tetrahydrofuran (THF) solution has maxima at 13380 cm^{-1} [ε = 13.9(7) × 10^3 M^{-1} cm^{-1}] and 29325 cm^{-1} [ε = 39(1) × 10^3 M^{-1} cm^{-1}] (Figure S2), with the former being blue-shifted relative to that for **3** (λ_{max} = 12400 cm^{-1}). The difference between the absorption maxima of **3** and **4** agrees with $\Delta E_{1/2}$ = 0.14 V from cyclic voltammetry measurements on **3** and **4** in THF ($E_{1/2}$ = −1.44 and −1.58 V vs Fc/Fc^+ for **3** and **4**, respectively; Figures S12 and S13).[14] Cyclic voltammograms of **2** are more complex than those of **3** or **4**, with a reversible one-electron process at −1.35 V versus Fc/Fc^+ followed by two broad irreversible features at ca. −1.55 and −1.7 V (Figures S10 and S11). The latter irreversible processes could arise from an ECE-type mechanism, although the nature of the chemical reaction step is unclear. In contrast to the heavier chalcogen-bridged congeners, we observe only a broad feature at 7364 cm^{-1} (ε = 2470 M^{-1} cm^{-1}) with a shoulder at 6480 cm^{-1} in UV/visible/NIR spectra of **2** (Figure S1). The spectral features for **2** and **4** are insensitive to solvent, as has been previously reported for **3**. A valence-delocalized pyrazolate-ligated $[Cu_3(\mu_3\text{-}O)]^{5+}$ cluster exhibits an asymmetric band at 9550 cm^{-1} (ε = 2600 M^{-1} cm^{-1}), which is attributed to an intervalence charge transfer (IVCT).[16b] This comparison

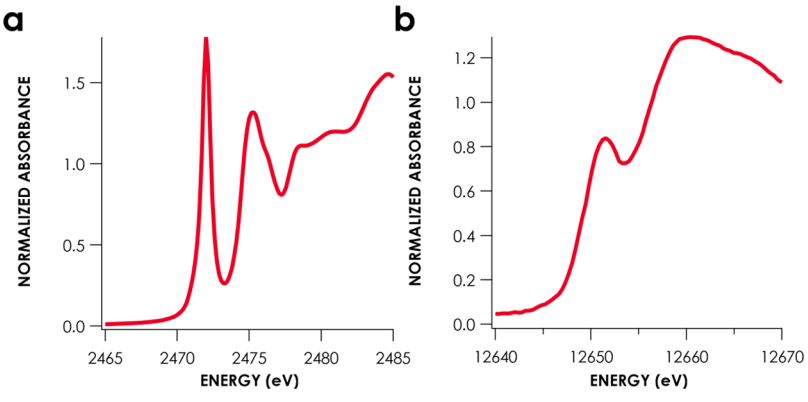

Figure 5. Ligand K-edge XAS of **3** and **4**. (a) S K-edge XAS of **3**. (b) Se K-edge XAS of **4**.

DOI: 10.1021/acs.inorgchem.8b01000
Inorg. Chem. 2018, 57, 11382–11392

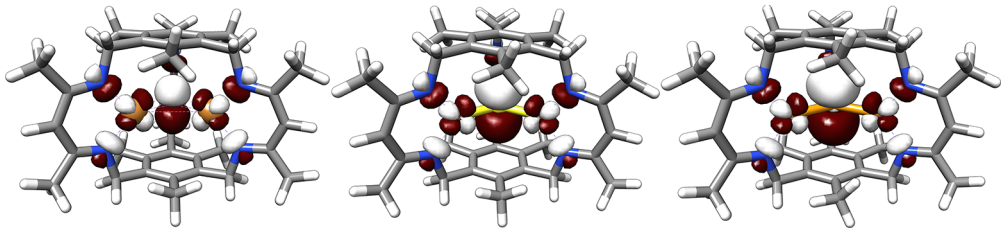

Figure 6. RKS DFT-calculated [PBE0/ZORA-def2-TZVP(-f) with CP(PPP) on Cu] SOMOs for **2′**−**4′**. Calculated basis orbital contributions to these MOs are printed along with experimentally determined values where available. Orbitals are printed at an isovalue of 0.03.

suggests that the long-wavelength absorptions in **2** and **4** may be IVCT in nature. As Di Francesco et al. previously noted[14] for **3**, however, these broad bands in spectra of **2** and **4** seemingly contraindicate canonical valence delocalization within the framework of a simplified two-state IVCT model and are more consistent with a charge-localized state.[25] Insofar as our NMR data and UV/visible/NIR data are inconclusive regarding an assignment of the extent of charge delocalization, we employed electronic structure calculations benchmarked to our experimental data to describe the nature of the bonding interactions in these $[Cu_3E]^{3+}$ cores.

Electronic Structure Calculations. Geometry optimizations were performed via both restricted Kohn−Sham (RKS) and broken-symmetry [BS(1,1)] density functional theory (DFT) and PBE0 hybrid DFT calculations on truncated models of **2**−**4** (**2′**−**4′**) in which the ethyl substituents on the benzene rings were replaced with methyl groups. The PBE0/def2-tzvp RKS solutions yielded structures most consistent with experimental metrical parameters derived by EXAFS or XRD (Table S4). Single-point calculations were then carried out [PBE0/ZORA-def2-tzvp(-f)] using the RKS coordinates. MO diagrams produced for **2**−**4** are qualitatively similar. In all cases, the LUMO is a_2'', ≈Cu $3d_{xz/yz}$ − E $2p_z$ π^*. These LUMOs and their admixture coefficients are reproduced in Figure 6. In general, there is excellent agreement between the experimental and DFT-calculated Cu 3d contributions to this LUMO. Although the S 3p character in the LUMO of **3** was the only ligand contribution that could be reliably quantified, this value too exhibits splendid agreement between the experimental (30.2%) and calculated (33.4%) values.

The aforementioned single points were then used as starting points for XAS predictions. Typically, such calculations are restricted to metal and ligand K-edge XAS, for which time-dependent DFT (TDDFT) produces results in good agreement with the experimental data.[26] However, TDDFT is inadequate for the prediction of $L_{2,3}$-edge XAS because it neglects the significant influence of core−hole spin−orbit coupling on these spectra. Attempts to simulate the Cu $L_{2,3}$-edge data using a ligand-field-multiplet model, supplemented with a charge-transfer-multiplet approximation, were unsuccessful. In contrast, DFT-ROCIS[40] (restricted open-shell configuration interaction singles) treatment of the Cu $L_{2,3}$-edge spectrum of **2** using the above RKS DFT electronic structure neatly describes the data. We note that our quantitative interpretation focuses on the Cu L_3-edge because the Cu L_2-edge is strongly influenced by processes that cannot be accounted for using this methodology (e.g., Auger decay, etc.).

Using DFT-ROCIS, we find a satisfactory agreement between the experimental and calculated Cu $L_{2,3}$-edge data for **2**−**4** following energy calibration. The trend in the energy observed experimentally of the main Cu L_3 lines of **2**−**4** is reproduced by DFT-ROCIS, although the calculated energies of the satellite features remain invariant for the three complexes. For **2**, there is a slight overestimation of the energy of the satellite feature found experimentally (+1.5 eV); however, the relative intensities of the main L_3 line versus the satellite feature are reproduced nicely (Figure S14). The DFT-ROCIS calculations reveal that the main L_3 line is comprised of 24 final states, while the satellite feature is comprised of 91 final states. The final states constituting the main line are almost exclusively Cu $2p_{3/2}$ → LUMO in character, while those comprising the satellite feature are admixtures of a number of Cu $2p_{3/2}$ transitions into higher-lying orbitals. We find that the average Cu 3d composition of the final states comprising the main line is 55.0%, whereas that of the satellite feature is 5.0%. Averaging over these states yields a total main-line-to-satellite Cu 3d ratio of ∼3:1, which is in reasonable agreement with the integrated experimentally observed main-line-to-satellite intensity ratio of 4.6:1. It should be noted that we have neglected the intensity contributions from Cu 2p → 4s excitations because, although formally allowed, we determined that the ⟨2p|4s⟩ overlap integral calculated for Cu in these compounds has ca. 1% the value of the corresponding ⟨2p|3d⟩ overlap integral. Thus, these excitations should minimally contribute to the observed intensity. For complex **3**, we find that both the main L_3 line and satellite feature are blue-shifted by +1.0 eV relative to the experimental data, while the main L_3 line and satellite feature calculated for **4** are blue-shifted by +0.8 eV relative to the experimental data. As with **2**, the DFT-ROCIS calculations also overestimate the degree of Cu character to the final states (the ratio of the average Cu 3d character to the main line/satellite feature are 49%:4.7% and 47%:5.0% for **3** and **4**, respectively). In other words, the calculated trends in the final state 3d character do not display as dramatic of a decrease as those observed experimentally. However, this is to be expected because DFT-ROCIS calculations do not capture additional physical processes, such as Auger emission, that contribute to defining the intensities of the L-edge peaks. Nevertheless, DFT-ROCIS adequately reproduces the experimentally observed trends in the experimental Cu $L_{2,3}$-edge data for these compounds.

DOI: 10.1021/acs.inorgchem.8b01000
Inorg. Chem. 2018, 57, 11382−11392

Although TDDFT could adequately reproduce the features of the K-edge spectra, we chose to use the DFT-ROCIS method to simulate the edge regions of the Cu K-edge XANES spectra for **2** for consistency (Figure 7). The pre-edge features

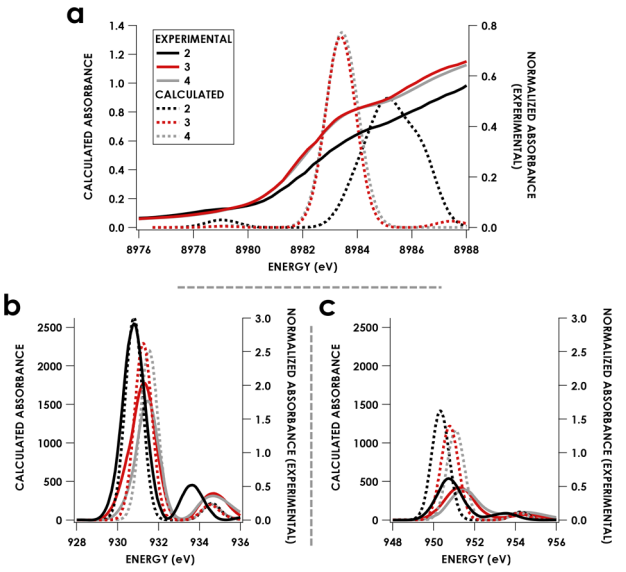

Figure 7. Experimental (solid) and DFT-ROCIS-calculated (dashed) Cu K-edge XAS (a) and $L_{2,3}$-edge XAS (b) of **2**–**4**. Scalar shifts of −4.2 eV and +7.6 eV were applied to the calculated K- and $L_{2,3}$-edge spectra, respectively.

of Cu K-edge XANES are attributed to excitations to states that arise almost exclusively because of Cu 1s → a_2'' LUMO transitions. These calculations also suggest that the higher-energy excitations, which are buried in the edge spectrum, are attributable to states with a high degree of multiconfigurational character and are comprised of orbitals that can best be described as transitions into states mostly comprised of Cu 4p and O 2p character. The DFT-ROCIS calculations also suggest that these transitions are present in the Cu K-edge XANES spectra of **3** and **4**. The DFT-ROCIS calculations yield low-energy transitions best described as Cu/S(Se) 1s → a_2'' LUMO transitions. These transitions are ∼5-fold weaker than the analogous Cu/O 1s → a_2'' LUMO found in **2**. This result suggests that these transitions would be too weak to observe in the experimental spectra of **3** and **4**, consistent with our experimental data. In contrast, the higher-energy transitions arising from excitations into Cu 4p/(S 3p)(Se 4p) states of **3** and **4** are more intense than the corresponding excitations into the Cu 4p/O 2p final states of **2**. These transitions calculated for **3** and **4** are also red-shifted relative to those calculated for **2**. Thus, the DFT-ROCIS-calculated Cu K-edge XAS spectra obtained for these complexes are consistent with the experimental data.

Despite its success in describing excited states accessed by core spectroscopy, DFT-ROCIS fails to provide meaningful agreement with the NIR spectral data. DFT-ROCIS predicts the low-energy bands at ∼7000 cm^{-1} found in the experimental NIR spectrum of **2** (Figure 8), but it also predicts three degenerate and one quasi-degenerate (34 cm^{-1} above the ground state) ground states, which is inconsistent with the NMR behavior of **2**. Consequently, a multireference calculation employing the spectroscopy-oriented configurational interaction (SORCI) method was carried out for **2′**. The

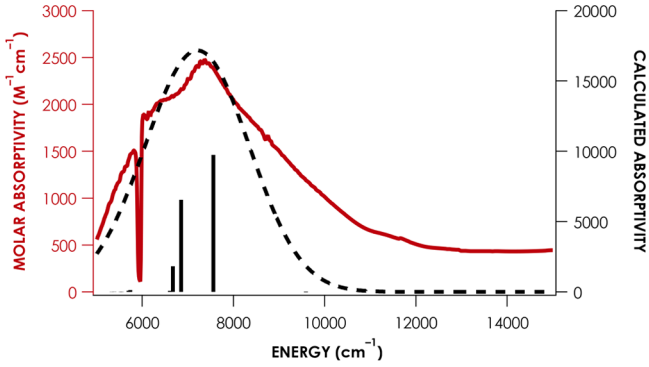

Figure 8. Experimental (red solid spectrum) and SORCI-calculated (black dashed spectrum) NIR absorption spectrum for **2**. The individual transitions produced by the SORCI calculation are given as gray sticks.

energies and compositions of five singlet and five triplet states were calculated using a complete active space CAS(14,10) reference. CAS(14,10) was chosen from a set of localized MOs involved in Cu−O bonding generated from RKS DFT using the PBE0 functional. Figure 8 exhibits the satisfactory agreement of the experimental NIR spectrum with the spectrum calculated via the SORCI procedure. Through detailed interpretation of the ground and excited states from the SORCI procedure, we have achieved a self-consistent electronic structure formulation that neatly accounts for all remaining spectroscopic observables.

The averaged atomic natural orbitals and their occupations comprising the CAS(14,10) used by the SORCI procedure are shown in Figure S15 and arranged in order of ground-state occupancy. CAS(14,10) captures 87% of the singlet ground-state references. Once again, the LUMO in the dominant (69%) ground-state configuration is predicted to be a Cu_3−O a_2'' antibonding combination, here comprising 15.9% O $2p_z$ with 75.4% Cu $3d_{xz/yz}$. The effectively degenerate e′ LUMO+1 and LUMO+2 sets in the dominant ground-state configuration comprise an average 11.2% Cu 3d contribution. Excitation into these orbitals would give rise to $L_{2,3}$ satellite features with a 1:3.4 intensity ratio to the main lines, in reasonable agreement with the experimental value of 1:4.6(1).

The compositions and relative energies of the singlet ground state and the four singlet and five triplet excited states produced by the SORCI calculation are compiled in Table S6. Transition energies are displayed in Table S7. The intense 7364 cm^{-1} NIR band in the experimental spectrum of **2** (Figures 8 and S1) is reproduced by a calculated feature near 7200 cm^{-1} principally comprising excitations to two singlet excited states, one at 7460 cm^{-1} and one at 6730 cm^{-1}. CAS(14,10) configurations describe 86% of these states, which are multiconfigurational in nature. These states are best described as electric-dipole-accessible $^1E'$ excited states arising as a result of excitations from predominantly Cu−Cu π^* e″ MOs to the Cu_3−O π^* a_2'' LUMO (Figure S15).

The ground-state electronic structure that emerges is thus characterized by delocalization of the electron vacancy over the three Cu and one O centers. On the basis of the above observations, we emphasize that a classical oxidation-state formulation (e.g., $Cu^ICu^{II}_2$ and O^{2-}) is an inadequate representation of the charge distribution in **2**. This system is highly covalent in nature, with nearly equal atomic orbital contributions between Cu and O atoms.

DOI: 10.1021/acs.inorgchem.8b01000
Inorg. Chem. 2018, 57, 11382−11392

Nature of the Cu_3–Chalcogen Bonds. On the basis of the above analysis, we find that not only do S-ligated **3** and Se-ligated **4** possess covalent Cu–E^{2-} interactions but also complex **2** displays a fairly high degree of covalent Cu–O bonding character. Two important insights into the Cu–chalcogen interactions can be gleaned from this observation. The first is that the oxidation-state formalism fails to properly describe the electronic structure of these clusters. Although it is tempting based on the absence of one valence electron, as determined by Cu $L_{2,3}$-edge XAS, to invoke a $Cu^{II}Cu^{I}_2$ configuration, the highly delocalized nature of the LUMO precludes such a clear-cut description. The $L_{2,3}$-edges show that ca. one 3d electron is absent from among the Cu centers and by necessity the remaining hole character is distributed across the chalcogen and N donors. The other noteworthy feature of this system is the fact that we find that the Cu–chalcogen bonding interactions observed in **2**–**4** are comparable to one another; the Cu–E^{2-} bonds found in all three compounds display significant covalent character. The differences in the electronegativities between S and Se are minimal, and thus one would predict similar bonding interactions found in **3** and **4**. O, on the other hand, is significantly more electronegative than both S and Se. Thus, one would predict considerable differences in the bonding interactions for **2** versus **3** and **4**, which is not observed; the bonding interactions in all three compounds follow a smooth continuum. In this homologous series of compounds, the bonding interactions observed between the chalcogens and Cu are similar to the more covalent bonding interactions that one would predict for a p-block metal as opposed to the dative bonding scheme that one would expect for transition-metal complexes. This study adds to a growing body of evidence that Cu occupies a unique position at the transition from 3d to the p-block metals, with the bonding picture transitioning from a classic ligand field to highly covalent and an inverted scheme.[7,8,11a,12] The flexibility in bonding as a function of the coordination environment is likely a key factor in the ability of Cu to perform a wide array of roles in biology, catalysis, and materials chemistry.

As mentioned above, Berry and co-workers employed spectroscopic and computational methods on a number of late-transition-metal dichalcogenide species, most notably $[CpNi]_2(E_2)$ and $[(TMEDA)Cu]_3(S_2)^{3+}$.[7,27] Their consensus bonding picture is one in which ligand oxidation is preferred to metal oxidation to the Ni^{III} or Cu^{III} state; that is, a subsulfide, S_2^{3-}, ligand bridges the metal centers rather than a more classical ligand-field treatment with two bridging chalcogenides (e.g., two μ_3-S^{2-}) and higher metal oxidation states (e.g., $2Cu^{II}$ and $1Cu^{III}$). Their analysis evidences the strongly covalent metal–chalcogen interactions in these compounds, reminiscent of ongoing discussions regarding oxocopper(III) versus oxylcopper(II). The covalency observed in the $[Cu_3E]^{3+}$ complexes reported here is consistent with these prior reports, with the important distinction that such covalency is observed without formally requiring Cu^{III} centers. Taken together, the arguments advanced by Berry and co-workers are repeated here but are not exclusive to formally high-valent oxidation states (e.g., Cu^{III} or Ni^{III}) and extend to more typical oxidation states of first-row late transition metals (e.g., Cu^{II} or Cu^{I}). Our results serve to reinforce that metal–ligand bonding in late-transition-metal chalcogen species is highly covalent such that formal oxidation-state assignments using classical ligand-field theory fail to accurately describe the electronic structures of these systems.

CONCLUSIONS

We have presented the detailed spectroscopic and computational study of a series of trinuclear Cu clusters, each possessing a covalent $[Cu_3(\mu_3\text{-}E)]^{3+}$ unit. This bonding picture synthesizes a suite of spectroscopic methods benchmarked to electronic structure calculations. Key observations are validation by the XAS and ESI-MS methods for the incorporation of the interstitial O and the Cu $L_{2/3}$-edge spectral analysis, which revealed a value of 50(1)% Cu 3d character in the LUMO. This composition of the LUMO and the experimental NIR data were faithfully reproduced in the CAS(14,10) calculation. Across the series, the contributions of the bonding interactions between the Cu 3d and chalcogen orbitals are analogous to each other. Although the degree of Cu character to the LUMO decreases as one progresses from the O to Se analogues, the 17% overall decrease is not dramatic.

Finally, we emphasize that a judicious choice of computational methods carefully benchmarked to a variety of experimental techniques is vital to obtaining any valid and meaningful insight into these systems. As electronic structure calculations become increasingly accessible, it has unfortunately become, accordingly, more common to encounter studies showcasing the "method of the moment" without proper consideration of the underlying chemical physics. In our present example, although hybrid DFT methods were successful in reproducing the geometry of **2**, these methods failed to accurately describe several of the spectroscopic properties of **2**. Furthermore, these methods yielded a representation of the electronic structure of **2** at odds with the experimental data. In fact, we found that there was no one computational approach that could reliably be applied to all aspects of this study. This study therefore highlights the importance of scrutinizing calculations used to interpret the experimental results.

EXPERIMENTAL SECTION

General Considerations. All reactions were performed under a N_2 atmosphere in an Innovative Technologies glovebox. Solvents were purchased from Sigma-Aldrich, dried using an Innovative Technologies solvent purification system, and then stored over activated 3 Å molecular sieves inside the N_2-filled glovebox. Reagents were purchased from Sigma-Aldrich or Strem Chemicals and used as received. Deuterated solvents were purchased from Cambridge Isotope Laboratories, purified according to reported procedures, and then stored over activated 3 Å molecular sieves. ^{1}H NMR spectra were collected on a Varian Inova spectrometer operating at 500 MHz for ^{1}H, equipped with a three-channel 5 mm indirect detection probe with *z*-axis gradients. All chemical shifts are reported in parts per million and referenced to tetramethylsilane for ^{1}H. ^{31}P NMR spectra were measured on a Bruker Mercury spectrometer operating at 300 MHz for ^{1}H. ESI-MS spectra were collected in positive mode by direct injection using a manual injector, which fed into a constant flow of anhydrous air-free solvent and then into an Agilent 6120 time-of-flight (TOF) spectrometer. The following ESI-MS conditions were used: gas temperature = 350 °C; fragmentation voltage = 120 V. UV/visible spectra were recorded on a Hewlett-Packard 8453 UV/visible spectrophotometer in anhydrous benzene, and UV/visible/NIR spectra were recorded on a PerkinElmer Lambda 900 double-path spectrophotometer in anhydrous benzene using quartz cuvettes having an air-free screw-top seal (Starna Cells Inc., Atascadero, CA). The ligand H_3L[28] and tricopper complex **1**[20] were synthesized as

DOI: 10.1021/acs.inorgchem.8b01000
Inorg. Chem. 2018, 57, 11382–11392

previously reported. Iodosobenzene was synthesized as described elsewhere.[29]

Cyclic voltammetry experiments were performed in a N_2 atmosphere glovebox using a Princeton Applied Research Versastat II potentiostat and a three-electrode setup (3 mm Pt button working electrode, Au wire counter electrode, and Ag/AgCl reference electrode) with electrodes purchased from BASi, Inc., and/or CH Instruments, Inc.

S K-edge XAS data were obtained on the Stanford Synchrotron Radiation Light Source (SSRL) beamline 4-3 under ring conditions of 3 GeV and 500 mA. Samples were prepared by grinding to a fine powder and spread to a vanishing thickness onto 38 μm low-S Mylar tape. All samples were measured in a He atmosphere at room temperature in fluorescence mode using a Lytle detector. The incident beam energy was calibrated by setting the energy of the first peak in the S K-edge spectrum of $Na_2S_2O_3{\cdot}5H_2O$ to 2472.02 eV. The intensity was normalized with respect to the incident beam using a He-filled ion chamber upstream of the sample. Data represent an average of three scans measured from 2400 to 2800 eV. Data were processed with *SIXpack*.[30] Spectra were normalized by fitting a polynomial flattened to energies below 2490 eV to the data and normalizing the region below 2490 eV to unity.

Synthesis of Cu_3OL (2). The following procedure is a representative example. A solution of **1** (200 mg, 0.220 mmol) in toluene (~15 mL) at 100 °C was added to a vial containing yellow iodosobenzene (70.0 mg, 0.318 mmol). The reaction was maintained at 100 °C with vigorous stirring for 5 min, during which the deep-red solution became dark-greenish-yellow in appearance. The reaction mixture was then quickly filtered through a Celite plug, which was pre-rinsed with hot toluene. The solvent was removed under reduced pressure. The residue was ground to a fine powder and further dried at 100 °C under vacuum for 2 h to remove residual iodobenzene. Dissolution of the residue in benzene, followed by lyophilization of the solvent, affords the product as a free-flowing powder (185 mg, 94%). For synthesis using trimethylamine *N*-oxide, the reaction was performed at room temperature over the course of 24 h and the product isolated in comparable yield as described above. IR (cm^{-1}): 2956, 1536, 1469, 1407, 1014, 730. ^{1}H NMR (300 MHz, toluene-d_8, 298 K): δ 1.47 (t, J = 7.33 Hz, 6 H), 1.88 (s, 18 H), 3.18 (q, J = 7.33 Hz, 12 H), 4.01 (s, 12 H), 4.50 (s, 3 H). ^{13}C NMR (101 MHz, C_6D_6, 298 K): δ 163.1, 141.2, 96.4, 49.4, 23.6, 23.0, 17.2. HR-ESI-MS (TOF). Calcd for $C_{45}H_{63}N_6Cu_3O$: m/z 894.2935 ($[M]^+$). Calcd for $C_{45}H_{64}N_6Cu_3O$: m/z 895.3014 ($[M + H]^+$). Found: m/z 895.3020.

Synthesis of Cu_3SL (3). The procedure used is a modified version of the previous report.[14] A 20 mL scintillation vial was charged with **1** (300 mg, 0.336 mmol) and toluene (~15 mL). This vial was heated to 100 °C. S_8 (25 mg, 0.781 mmol) was added to a separate 20 mL vial equipped with a poly(tetrafluoroethylene) magnetic stir bar. The hot toluene solution of **1** was rapidly added to the stirring the vial containing S_8 and the reaction maintained at 100 °C. Upon mixing, the reaction mixture evolved to an emerald-green mixture. The reaction was stirred at 100 °C for 5 min and then rapidly filtered through pre-rinsed Celite while hot and through a ground-glass fritted funnel (fine porosity) packed with Celite, and the green filtrate was collected. Volatiles were removed under reduced pressure to yield a microcrystalline green solid. Dissolution in benzene and subsequent lyophilization of a frozen benzene solution under reduced pressure yielded **2** as a spectroscopically pure green powder (145 mg, 48%). NMR, IR, and ESI-MS data were indistinguishable from those reported previously.

Synthesis of Cu_3SeL (4). Synthesis was carried out like that for **3** with the following modifications. After the preheated solution of **1** (300 mg, 0.336 mmol) in toluene (~15 mL) was mixed with Se metal (60 mg, 0.760 mmol), the reaction mixture was allowed to stir at 100 °C for 2 h, over which time a gradual color change from dark red to dark green was observed. The workup was like that for **3**, yielding the selenide congener **4** as a forest-green powder (270 mg, 86%). Single crystals suitable for XRD were obtained from slow evaporation of a saturated benzene solution at 25 °C. IR (cm^{-1}): 2959, 1524, 1404, 1329, 1012. ^{1}H NMR (500 MHz, C_6D_6, 298 K): δ 4.97 (s, 3H, C*H*), 4.51 (s, 12H, N−CH_2), 2.70 (q, $^3J_{H-H}$ = 7.5 Hz, 12H, CH_2CH$_3$), 2.07 (s, 18H, CCH_3), 1.14 (t, $^3J_{H-H}$ = 7.5 Hz, 18H, CH$_2$CH_3). ^{13}C NMR (101 MHz, toluene-d_8, 298 K): δ 164.4, 143.7, 138.1, 98.0, 50.8, 23.1, 22.4, 16.5. HR-ESI-MS (TOF). Calcd for $C_{45}H_{64}N_6Cu_3Se$: m/z 959.2233 ($[M + H]^+$). Found: m/z 959.2256.

Reactivity Studies of 2. An analogous procedure was employed for trimethylphosphine, tris(*tert*-butylphosphine), triphenylphosphine, dihydroanthracene, 2,6-di-*tert*-butylphenol, xanthene, styrene, cyclohexene, and ethylmethyl sulfide, with the exception of propylene. Ethylmethyl sulfide (0.8 μL, 9 μmol) and **2** (3.0 mg, 3.3 μmol) were dissolved in benzene-d_6 (~0.4 mL) in an NMR tube and then removed from the glovebox. ^{1}H or ^{31}P NMR spectra were then recorded after 30 min and 24 h. For propylene, **2** (3.0 mg, 3.3 μmol) was dissolved in benzene-d_6 (~0.4 mL) in a J. Young NMR tube and then transferred to a vacuum manifold. A freeze−pump−thaw cycle was then carried out on the sample, after which the tube was refilled with propylene to ~1 atm. ^{1}H NMR spectra were recorded as noted for other substrates.

Cu and Se K-Edge XAS. Solid samples of Cu_3OL, Cu_3SeL, and **1** were finely ground in boron nitride and placed in 1 mm aluminum sample holders between 37 μm Kapton tape windows. Data were obtained in transmission mode using N_2-filled ionization chambers on the SSRL beamline 2-2 under ring conditions of 3 GeV and 500 mA. Light was monochromated using a Si(111) double monochromator, which was detuned 40% to eliminate higher-order harmonics. Samples were maintained at 20 K throughout data collection with the use of a He Displex closed-cycle cryostat.

For the Cu K-edge data, spectra were calibrated against the simultaneously recorded spectrum of a Cu foil standard, with the first inflection point set to 8980.3 eV. The monochromator position displayed no perceptible drift during data analysis, with the resulting measured energy difference being <0.1 eV from spectrum to spectrum. XANES data were obtained in 10 eV steps in the pre-edge region (8779−8969 eV), 0.3 eV steps in the edge region (8969−8999 eV), and 0.5 eV steps in the near-edge region (8999−9129 eV). Each data set represents the sum of three individual data sets. EXAFS data were collected in 10 eV steps in the pre-edge region (8779−8969 eV), 0.5 eV steps in the edge region (8969−8989 eV), 1 eV steps in the near-edge region (8989−9009 eV), and 0.05K eV steps in the far-edge region (9009−16.5K). Data were worked-up and analyzed using the XAS analysis package *EXAFS123*.[31] Prior to the baseline fitting, all known monochromator glitches were removed from the XAS spectra. The pre-edge background was removed from the averaged spectra by fitting the pre-edge region to a polynomial function. The background in the EXAFS region was fit to a third-order spline function. EXAFS data were modeled using the single scatter approximation with phase and amplitude files generated with *FEFF v8.2* as previously described.[32]

For Se K-edge data, spectra were calibrated against the simultaneously recorded spectrum of an elemental Se standard, with the first inflection point set to 12658 eV. Data were obtained in 10 eV steps in the pre-edge region (12458−12645 eV), 0.3 eV steps in the edge region (12645−12678 eV), and 0.5 eV steps in the near-edge region (12678−12758 eV). Data were then processed as outlined above.

Soft XAS. A solid sample of Cu_3OL was spread onto conductive C tape mounted on an Al sample rod. Cu $L_{2,3}$-edge XAS data were collected on the SSRL beamline 10-1 under ring conditions of 3 GeV and 500 mA. Data were collected in fluorescence mode. Four scans were measured from 910 to 975 eV, each was normalized to incident X-ray flux as measured using the photocurrent of a Au grid reference monitor, and these scans were averaged and processed using *PyMca*. For both Cu $L_{2,3}$ XAS data, the pre-edge background was removed from the averaged spectrum by fitting a linear fit to the pre-edge region (Cu: 920−925 eV) and subtracting this line from the entire spectrum. A linear spline was fit from 965 to 975 eV, and this line was subtracted from the data, which were then normalized to a value of 1.0 at 965 eV. For Cu $L_{2,3}$, the energy was calibrated using published values for the L_3 and L_2 peaks of CuF_2 at 930.5 and 950.5 eV. CuF_2

DOI: 10.1021/acs.inorgchem.8b01000
Inorg. Chem. 2018, 57, 11382−11392

was measured before and after data collection, and averaged values were used for the calibration.

Electronic Structure Calculations. Electronic structure calculations were performed using the software package *ORCA v3.03*.[33] DFT was performed using the def2-tzvp basis set on all atoms and the atom pairwise dispersion correction with Becke−Johnson damping to account for dispersive interactions.[34] ORCA VeryTightSCF convergence criteria were used for the self-consistent-fieldcycles, with program defaults used for all other convergence criteria and settings.[33] Both restricted-closed-shell and broken-symmetry solutions were considered. Geometry optimizations were performed at the BP86 level[35] and used the resolution of the identity (RI) approximation and def2-tzvp/c auxiliary basis set.[36] Single-point calculations were performed at the PBE0 level[37] and used the RIJCOSX approximation and def2-tzvp/j auxiliary basis set.[38] For calculation of the XAS spectra, both BS and RKS solutions were utilized at the PBE0 level. Each yielded good agreement with the experimental data. Calculations employed the def2-tzvp(-f) basis set and zeroth-order regular approximation (ZORA).[34b,39] Cu K and $L_{2,3}$-edge XAS data were calculated using DFT-ROCIS.[40] For each Cu $L_{2,3}$-edge calculation and the Cu K-edge calculations, the first 50 roots were examined. DFT-ROCIS employed Coulomb (c_1 = 0.21), exchange (c_2 = 0.49), and off-diagonal configuration interaction matrix scaling parameters (c_3 = 0.29) previously defined for the B3LYP functional. Cu K-edge spectra were simulated by employing a −4.6 eV shift to all transitions, applying a Gaussian line shape to each transition (fwhm = 1.3 eV), and summing each individual transition. Cu L-edge spectra were simulated by employing a +7.6 eV shift to all transitions, applying a Gaussian line shape to each transition (fwhm = 1.0 eV), and summing each individual transition.

The multireference character in the ground state of **2** was assessed with SORCI[41] calculations. SORCI was performed on a CAS for truncated **2** (Cu_3OL^{Me}) comprising 10 electrons and 8 orbitals [CAS(14,10)]. The def2-SVP-ZORA basis set was used on all atoms except for H atoms, for which the MINIX basis set was used.[42] The ZORA relativistic correction was used in all SORCI calculations. As described elsewhere,[41] individual selection was used to ease the computational burden. The size of the first-order interacting space was reduced with a threshold: $T_{sel} = 10^{-6}E_h$. A further approximation involved reducing the reference space through another selection: all initial references that contributed less than a second threshold ($T_{pre} = 10^{-5}$) to the zeroth-order states were rejected from the reference space. Starting orbitals were taken from RKS orbitals generated via a PBE0 calculation.

■ ASSOCIATED CONTENT

Supporting Information

The Supporting Information is available free of charge on the ACS Publications website at DOI: 10.1021/acs.inorgchem.8b01000.

Spectral (^{1}H NMR, UV/visible, and NIR) data for **2**−**4**, electrochemical data for **2**−**4**, SORCI for **2**, raw and fit Cu $L_{2,3}$-edge XAS of **2**−**4**, and sample O-atom-transfer reactivity of **2** (PDF)

Accession Codes

CCDC 1821029 contains the supplementary crystallographic data for this paper. These data can be obtained free of charge via www.ccdc.cam.ac.uk/data_request/cif, or by emailing data_request@ccdc.cam.ac.uk, or by contacting The Cambridge Crystallographic Data Centre, 12 Union Road, Cambridge CB2 1EZ, UK; fax: +44 1223 336033.

■ AUTHOR INFORMATION

Corresponding Authors

*E-mail: murray@chem.ufl.edu (L.J.M.).
*E-mail: kml236@cornell.edu (K.M.L.).
*E-mail: jshearer@trinity.edu (J.S.).

ORCID

Vincent J. Catalano: 0000-0003-2151-2892
Kyle M. Lancaster: 0000-0001-7296-128X
Jason Shearer: 0000-0001-7469-7304
Leslie J. Murray: 0000-0002-1568-958X

Present Address

△Department of Chemistry, Trinity University, San Antonio, Texas 78212-7200, United States

Author Contributions

‡These authors contributed equally.

Notes

The authors declare no competing financial interest.

■ ACKNOWLEDGMENTS

The authors graciously acknowledge support from the following: National Science Foundation Grants CAREER CHE-1454455 (K.M.L.), CHE-1464876 (L.J.M.), CHE-1048604 (University of Florida), and CHE-1565766 (J.S.) and 52704-DNI3 (L.J.M.); National Institutes of Health Grant R15-GM120641-01 (J.S.); Alfred P. Sloan Foundation (K.M.L.). R.B.F. was supported by a University of Florida Graduate Research Fellowship. L.J.M. thanks Prof J. Gardinier for acquiring NIR spectra. XAS data were obtained at the SSRL, which is supported by the U.S. Department of Energy, Office of Science, Office of Basic Energy Sciences, under Contract DE-AC02-76SF00515. The SSRL Structural Molecular Biology Program is supported by the Department of Energy's Office of Biological and Environmental Research and by the NIH/NIGMS (including P41GM103393).

■ REFERENCES

(1) (a) Xia, Z.; Fang, H.; Zhang, X.; Molokeev, M. S.; Gautier, R.; Yan, Q.; Wei, S.-H.; Poeppelmeier, K. R. $CsCu_5Se_3$: A Copper-Rich Ternary Chalcogenide Semiconductor with Nearly Direct Band Gap for Photovoltaic Application. *Chem. Mater.* **2018**, *30*, 1121. (b) Coughlan, C.; Ibáñez, M.; Dobrozhan, O.; Singh, A.; Cabot, A.; Ryan, K. M. Compound Copper Chalcogenide Nanocrystals. *Chem. Rev.* **2017**, *117* (9), 5865−6109.

(2) (a) Singh, A.; Singh, S.; Levcenko, S.; Unold, T.; Laffir, F.; Ryan, K. M. Compositionally Tunable Photoluminescence Emission in $Cu_2ZnSn(S_{1-x}Se_x)_4$ Nanocrystals. *Angew. Chem., Int. Ed.* **2013**, *52* (35), 9120−9124. (b) Comin, A.; Manna, L. New Materials for Tunable Plasmonic Colloidal Nanocrystals. *Chem. Soc. Rev.* **2014**, *43* (11), 3957−3975. (c) Niezgoda, J. S.; Rosenthal, S. J. Synthetic Strategies for Semiconductor Nanocrystals Expressing Localized Surface Plasmon Resonance. *ChemPhysChem* **2016**, *17* (5), 645−653. (d) Willhammar, T.; Sentosun, K.; Mourdikoudis, S.; Goris, B.; Kurttepeli, M.; Bercx, M.; Lamoen, D.; Partoens, B.; Pastoriza-Santos, I.; Pérez-Juste, J.; Liz-Marzán, L. M.; Bals, S.; Van Tendeloo, G. Structure and Vacancy Distribution in Copper Telluride Nanoparticles Influence Plasmonic Activity in the Near-Infrared. *Nat. Commun.* **2017**, *8*, 14925. (e) Kriegel, I.; Jiang, C.; Rodríguez-Fernández, J.; Schaller, R. D.; Talapin, D. V.; da Como, E.; Feldmann, J. Tuning the Excitonic and Plasmonic Properties of Copper Chalcogenide Nanocrystals. *J. Am. Chem. Soc.* **2012**, *134* (3), 1583−1590. (f) Kriegel, I.; Rodríguez-Fernández, J.; Wisnet, A.; Zhang, H.; Waurisch, C.; Eychmüller, A.; Dubavik, A.; Govorov, A. O.; Feldmann, J. Shedding Light on Vacancy-Doped Copper Chalcogenides: Shape-Controlled Synthesis, Optical Properties, and Modeling of Copper Telluride Nanocrystals with Near-Infrared Plasmon Resonances. *ACS Nano* **2013**, *7* (5), 4367−4377. (g) Llorente, V. B.; Dzhagan, V. M.; Gaponik, N.; Iglesias, R. A.; Zahn, D. R. T.; Lesnyak, V. Electrochemical Tuning of Localized

DOI: 10.1021/acs.inorgchem.8b01000
Inorg. Chem. 2018, 57, 11382−11392

Surface Plasmon Resonance in Copper Chalcogenide Nanocrystals. *J. Phys. Chem. C* **2017**, *121* (33), 18244−18253.
(3) (a) Kashida, S.; Shimosaka, W.; Mori, M.; Yoshimura, D. Valence Band Photoemission Study of the Copper Chalcogenide Compounds, Cu_2S, Cu_2Se and Cu_2Te. *J. Phys. Chem. Solids* **2003**, *64* (12), 2357−2363. (b) Davletshina, A. D.; Yakshibaev, R. A.; Bikkulova, N. N.; Stepanov, Y. M.; Bikkulova, L. V. Ab initio Calculations of Band Structure of Solid Solutions of Copper and Silver Chalcogenides. *Solid State Ionics* **2014**, *257*, 29−31. (c) Ghosh, A.; Biswas, A.; Thangavel, R.; Udayabhanu, G. Photo-Electrochemical Properties and Electronic Band Structure of Kesterite Copper Chalcogenide Cu_2-II-Sn-S_4 (II = Fe, Co, Ni) thin films. *RSC Adv.* **2016**, *6* (98), 96025−96034.
(4) Grundner, S.; Markovits, M. A. C.; Li, G.; Tromp, M.; Pidko, E. A.; Hensen, E. J. M.; Jentys, A.; Sanchez-Sanchez, M.; Lercher, J. A. Single-Site Trinuclear Copper Oxygen Clusters in Mordenite for Selective Conversion of Methane to Methanol. *Nat. Commun.* **2015**, *6*, 7546.
(5) Brown, E. C.; York, J. T.; Antholine, W. E.; Ruiz, E.; Alvarez, S.; Tolman, W. B. $[Cu_3(\mu\text{-}S)_2]^{3+}$ Clusters Supported by N-Donor Ligands: Progress Toward a Synthetic Model of the Catalytic Site of Nitrous Oxide Reductase. *J. Am. Chem. Soc.* **2005**, *127*, 13752−13753.
(6) (a) Elwell, C. E.; Gagnon, N. L.; Neisen, B. D.; Dhar, D.; Spaeth, A. D.; Yee, G. M.; Tolman, W. B. Copper−Oxygen Complexes Revisited: Structures, Spectroscopy, and Reactivity. *Chem. Rev.* **2017**, *117*, 2059−2107. (b) Vanelderen, P.; Snyder, B. E. R.; Tsai, M. L.; Hadt, R. G.; Vancauwenbergh, J.; Coussens, O.; Schoonheydt, R. A.; Sels, B. F.; Solomon, E. I. Spectroscopic Definition of the Copper Active Sites in Mordenite: Selective Methane Oxidation. *J. Am. Chem. Soc.* **2015**, *137* (19), 6383−6392. (c) Woertink, J. S.; Smeets, P. J.; Groothaert, M. H.; Vance, M. A.; Sels, B. F.; Schoonheydt, R. A.; Solomon, E. I. A $[Cu_2O]^{2+}$ Core in Cu-ZSM-5, the Active Site in the Oxidation of Methane to Methanol. *Proc. Natl. Acad. Sci. U. S. A.* **2009**, *106* (45), 18908−18913. (d) Kim, S.; Stahlberg, J.; Sandgren, M.; Paton, R. S.; Beckham, G. T. Quantum Mechanical Calculations Suggest that Lytic Polysaccharide Monooxygenases use a Copper-Oxyl, Oxygen-Rebound Mechanism. *Proc. Natl. Acad. Sci. U. S. A.* **2014**, *111* (1), 149−154. (e) Lewis, E. A.; Tolman, W. B. Reactivity of Dioxygen−Copper Systems. *Chem. Rev.* **2004**, *104*, 1047−1076.
(7) Berry, J. F. Two-Center/Three-Electron Sigma Half-Bonds in Main Group and Transition Metal Chemistry. *Acc. Chem. Res.* **2016**, *49* (1), 27−34.
(8) Sarangi, R.; Yang, L.; Winikoff, S. G.; Gagliardi, L.; Cramer, C. J.; Tolman, W. B.; Solomon, E. I. X-ray Absorption Spectroscopic and Computational Investigation of a Possible S···S Interaction in the $[Cu_3S_2]^{3+}$ Core. *J. Am. Chem. Soc.* **2011**, *133* (43), 17180−17191.
(9) (a) Himes, R. A.; Karlin, K. D. A New Copper-Oxo Player in Methane Oxidation. *Proc. Natl. Acad. Sci. U. S. A.* **2009**, *106* (45), 18877−18878. (b) Lee, J. Y.; Karlin, K. D. Elaboration of Copper−Oxygen Mediated C−H Activation Chemistry in Consideration of Future Fuel and Feedstock Generation. *Curr. Opin. Chem. Biol.* **2015**, *25*, 184−193. (c) Solomon, E. I.; Heppner, D. E.; Johnston, E. M.; Ginsbach, J. W.; Cirera, J.; Qayyum, M.; Kieber-Emmons, M. T.; Kjaergaard, C. H.; Hadt, R. G.; Tian, L. Copper Active Sites in Biology. *Chem. Rev.* **2014**, *114*, 3659.
(10) (a) Donoghue, P. J.; Tehranchi, J.; Cramer, C. J.; Sarangi, R.; Solomon, E. I.; Tolman, W. B. Rapid C-H Bond Activation by a Monocopper(III)-Hydroxide Complex. *J. Am. Chem. Soc.* **2011**, *133* (44), 17602−17605. (b) Dhar, D.; Yee, G. M.; Spaeth, A. D.; Boyce, D. W.; Zhang, H.; Dereli, B.; Cramer, C. J.; Tolman, W. B. Perturbing the Copper(III)-Hydroxide Unit through Ligand Structural Variation. *J. Am. Chem. Soc.* **2016**, *138* (1), 356−368. (c) Dhar, D.; Tolman, W. B. Hydrogen Atom Abstraction from Hydrocarbons by a Copper(III)-Hydroxide Complex. *J. Am. Chem. Soc.* **2015**, *137* (3), 1322−1329.
(11) (a) Walroth, R. C.; Lukens, J. T.; MacMillan, S. N.; Finkelstein, K. D.; Lancaster, K. M. Spectroscopic Evidence for a 3d(10) Ground State Electronic Configuration and Ligand Field Inversion in $[Cu(CF_3)_4]^{1-}$. *J. Am. Chem. Soc.* **2016**, *138* (6), 1922−1931. (b) Tomson, N. C.; Williams, K. D.; Dai, X.; Sproules, S.; DeBeer, S.; Warren, T. H.; Wieghardt, K. Re-Evaluating the Cu K Pre-Edge XAS Transition in Complexes with Covalent Metal−Ligand Interactions. *Chem. Sci.* **2015**, *6* (4), 2474−2487.
(12) Hoffmann, R.; Alvarez, S.; Mealli, C.; Falceto, A.; Cahill, T. J.; Zeng, T.; Manca, G. From Widely Accepted Concepts in Coordination Chemistry to Inverted Ligand Fields. *Chem. Rev.* **2016**, *116* (14), 8173−8192.
(13) (a) Bakhoda, A.; Jiang, Q.; Bertke, J. A.; Cundari, T. R.; Warren, T. H. Elusive Terminal Copper Arylnitrene Intermediates. *Angew. Chem., Int. Ed.* **2017**, *56* (23), 6426−6430. (b) Aguila, M. J. B.; Badiei, Y. M.; Warren, T. H. Mechanistic Insights into C−H Amination via Dicopper Nitrenes. *J. Am. Chem. Soc.* **2013**, *135* (25), 9399−9406. (c) King, E. R.; Hennessy, E. T.; Betley, T. A. Catalytic C−H Bond Amination from High-Spin Iron Imido Complexes. *J. Am. Chem. Soc.* **2011**, *133* (13), 4917−4923. (d) Wilding, M. J. T.; Iovan, D. A.; Betley, T. A. High-Spin Iron Imido Complexes Competent for C−H Bond Amination. *J. Am. Chem. Soc.* **2017**, *139* (34), 12043−12049. (e) Wilding, M. J. T.; Iovan, D. A.; Wrobel, A. T.; Lukens, J. T.; MacMillan, S. N.; Lancaster, K. M.; Betley, T. A. Direct Comparison of C−H Bond Amination Efficacy through Manipulation of Nitrogen-Valence Centered Redox: Imido versus Iminyl. *J. Am. Chem. Soc.* **2017**, *139* (41), 14757−14766.
(14) Di Francesco, G. N.; Gaillard, A.; Ghiviriga, I.; Abboud, K. A.; Murray, L. J. Modeling Biological Copper Clusters: Synthesis of a Tricopper Complex, and Its Chloride- and Sulfide-Bridged Congeners. *Inorg. Chem.* **2014**, *53* (9), 4647−4654.
(15) (a) Johnson, B. J.; Antholine, W. E.; Lindeman, S. V.; Graham, M. J.; Mankad, N. P. A One-Hole Cu_4S Cluster with N_2O Reductase Activity: A Structural and Functional Model for CuZ*. *J. Am. Chem. Soc.* **2016**, *138* (40), 13107−13110. (b) Zhai, J.; Filatov, A. S.; Hillhouse, G. L.; Hopkins, M. D. Synthesis, Structure, and Reactions of a Copper-Sulfido Cluster Comprised of the Parent Cu_2S Unit. $\{(NHC)Cu\}_2(\mu\text{-}S)$. *Chem. Sci.* **2016**, *7* (1), 589−595. (c) Bagherzadeh, S.; Mankad, N. P. Oxidation of a $[Cu_2S]$ Complex by N_2O and CO_2: Insights into a Role of Tetranuclearity in the CuZ Site of Nitrous Oxide Reductase. *Chem. Commun.* **2018**, *54* (9), 1097−1100. (d) Zhai, J.; Hopkins, M. D.; Hillhouse, G. L. Synthesis and Structure of a Cu^{I}_3S Cluster Unsupported by Other Bridging Ligands. *Organometallics* **2015**, *34* (19), 4637−4640.
(16) (a) Rivera-Carrillo, M.; Chakraborty, I.; Mezei, G.; Webster, R. D.; Raptis, R. G. Tuning of the $[Cu_3(\mu\text{-}O)^{4+/5+}]$ Redox Couple: Spectroscopic Evidence Charge Delocalization in the $[Cu_3(\mu\text{-}O)^{5+}]$ Mixed-Valent Species. *Inorg. Chem.* **2008**, *47* (17), 7644−7650. (b) Mezei, G.; McGrady, J. E.; Raptis, R. G. First Structural Characterization of a Delocalized, Mixed-Valent, Triangular Cu_3^{7+} Species: Chemical and Electrochemical Oxidation of a $Cu^{II}_3(\mu_3\text{-}O)$ Pyrazolate and Electronic Structure of the Oxidation Product. *Inorg. Chem.* **2005**, *44* (21), 7271−7273. (c) Suh, M. P.; Han, M. Y.; Lee, J. H.; Min, K. S.; Hyeon, C. One-Pot Template Synthesis and Properties of a Molecular Bowl: Dodecaaza Macrotetracycle with μ_3-oxo and μ_3-Hydroxo Tricopper(II) Cores. *J. Am. Chem. Soc.* **1998**, *120* (15), 3819−3820.
(17) Heppner, D. E.; Kjaergaard, C. H.; Solomon, E. I. Mechanism of the Reduction of the Native Intermediate in the Multicopper Oxidases: Insights into Rapid Intramolecular Electron Transfer in Turnover. *J. Am. Chem. Soc.* **2014**, *136* (51), 17788−17801.
(18) (a) Li, B.; Li, J.; Liu, R.; Zhu, H.; Roesky, H. W. Facile Route to Rare Heterobimetallic Aluminum−Copper and Aluminum−Zinc Selenide Clusters. *Inorg. Chem.* **2017**, *56* (6), 3136−3139. (b) Kimani, M. M.; Brumaghim, J. L.; VanDerveer, D. Probing the Antioxidant Action of Selenium and Sulfur Using Cu(I)-Chalcogenone Tris-(pyrazolyl)methane and -borate Complexes. *Inorg. Chem.* **2010**, *49* (20), 9200−9211. (c) Azizpoor Fard, M.; Levchenko, T. I.; Cadogan, C.; Humenny, W. J.; Corrigan, J. F. Stable -ESiMe3 Complexes of Cu^{I} and Ag^{I} (E = S, Se) with NHCs: Synthons in Ternary Nanocluster Assembly. *Chem. - Eur. J.* **2016**, *22* (13), 4543−4550. (d) Tan, G.; Xiong, Y.; Inoue, S.; Enthaler, S.; Blom, B.; Epping, J. D.; Driess, M. From Elusive Thio- and Selenosilanoic Acids to Copper(I)

DOI: 10.1021/acs.inorgchem.8b01000
Inorg. Chem. 2018, 57, 11382−11392

Complexes with Intermolecular Si = E → Cu-O-Si Coordination Modes (E = S, Se). *Chem. Commun.* **2013**, *49* (49), 5595−5597.
(19) Kau, L. S.; Spira-Solomon, D. J.; Penner-Hahn, J. E.; Hodgson, K. O.; Solomon, E. I. X-ray Absorption Edge Determination of the Oxidation State and Coordination Number of Copper. Application to the Type 3 site in Rhus Vernicifera Laccase and its Reaction with Oxygen. *J. Am. Chem. Soc.* **1987**, *109* (21), 6433−6442.
(20) Murray, L. J.; Weare, W. W.; Shearer, J.; Mitchell, A. D.; Abboud, K. A. Isolation of a (Dinitrogen)Tricopper(I) Complex. *J. Am. Chem. Soc.* **2014**, *136* (39), 13502−13505.
(21) Sarangi, R.; Aboelella, N.; Fujisawa, K.; Tolman, W. B.; Hedman, B.; Hodgson, K. O.; Solomon, E. I. X-ray Absorption Edge Spectroscopy and Computational Studies on $LCuO_2$ Species: Superoxide−Cu^{II} versus Peroxide−Cu^{III} Bonding. *J. Am. Chem. Soc.* **2006**, *128* (25), 8286−8296.
(22) Walroth, R. C.; Uebler, J. W.; Lancaster, K. M. Probing Cu^{I} in Homogeneous Catalysis using High-Energy-Resolution Fluorescence-Detected X-ray Absorption Spectroscopy. *Chem. Commun.* **2015**, *51* (48), 9864−9867.
(23) (a) DuBois, J. L.; Mukherjee, P.; Stack, T. D. P.; Hedman, B.; Solomon, E. I.; Hodgson, K. O. A systematic K-edge X-ray Absorption Spectroscopic Study of Cu(III) Sites. *J. Am. Chem. Soc.* **2000**, *122* (24), 5775−5787. (b) George, S. J.; Lowery, M. D.; Solomon, E. I.; Cramer, S. P. Copper L-edge Spectral Studies: A Direct Experimental Probe of the Ground-State Covalency in the Blue Copper Site in Plastocyanin. *J. Am. Chem. Soc.* **1993**, *115* (7), 2968−2969.
(24) Sarangi, R.; DeBeer George, S.; Rudd, D. J.; Szilagyi, R. K.; Ribas, X.; Rovira, C.; Almeida, M.; Hodgson, K. O.; Hedman, B.; Solomon, E. I. Sulfur K-Edge X-ray Absorption Spectroscopy as a Probe of Ligand−Metal Bond Covalency: Metal vs Ligand Oxidation in Copper and Nickel Dithiolene Complexes. *J. Am. Chem. Soc.* **2007**, *129* (8), 2316−2326.
(25) D'Alessandro, D. M.; Keene, F. R. Current Trends and Future Challenges in the Experimental, Theoretical and Computational Analysis of Intervalence Charge Transfer (IVCT) Transitions. *Chem. Soc. Rev.* **2006**, *35* (5), 424−440.
(26) DeBeer George, S.; Petrenko, T.; Neese, F. Prediction of Iron K-Edge Absorption Spectra Using Time-Dependent Density Functional Theory. *J. Phys. Chem. A* **2008**, *112*, 12936−12943.
(27) (a) Yao, S. A.; Lancaster, K. M.; Götz, A. W.; DeBeer, S.; Berry, J. F. X-ray Absorption Spectroscopic, Crystallographic, Theoretical (DFT) and Chemical Evidence for a Chalcogen−Chalcogen Two-Center/Three-Electron Half Bond in an Unprecedented "Subselenide" Se_2^{3-} Ligand. *Chem. - Eur. J.* **2012**, *18* (30), 9179−9183. (b) Berry, J. F. A Definitive Answer to a Bonding Quandary? The Role of One-Electron Resonance Structures in the Bonding of a $\{Cu_3S_2\}^{3+}$ Core. *Chem. - Eur. J.* **2010**, *16* (9), 2719−2724. (c) Yao, S. A.; Martin-Diaconescu, V.; Infante, I.; Lancaster, K. M.; Götz, A. W.; DeBeer, S.; Berry, J. F. Electronic Structure of Ni_2E_2 Complexes (E = S, Se, Te) and a Global Analysis of M_2E_2 Compounds: A Case for Quantized E_2^{n-} Oxidation Levels with n = 2, 3, or 4. *J. Am. Chem. Soc.* **2015**, *137* (15), 4993−5011.
(28) Guillet, G. L.; Sloane, F. T.; Ermert, D. M.; Calkins, M. W.; Peprah, M. K.; Knowles, E. S.; Cizmar, E.; Abboud, K. A.; Meisel, M. W.; Murray, L. J. Preorganized Assembly of Three Iron(II) or Manganese(II) μ-diketiminate Complexes Using a Cyclophane Ligand. *Chem. Commun.* **2013**, *49* (59), 6635−6637.
(29) Moriarty, R. M. K.; Jerome, W., II; Zhdankin, V. V.; Courillon, C.; Lacote, E.; Malacria, M.; Darses, B.; Dauban, P. Iodosylbenzene. *e-EROS Encyclopedia of Reagents for Organic Synthesis*; John Wiley and Sons, 2012; pp 1−17.
(30) Webb, S. M. SIXpack: a graphical user interface for XAS analysis using IFEFFIT. *Phys. Scr.* **2005**, *2005* (T115), 1011.
(31) Shearer, J. S.; Scarrow, R. *EXAFS123: A Software Package for the Work-up, Analysis and Plotting of X-ray Absorption Data*; University of Nevada, Reno: Reno, NV, 2007.
(32) (a) Ankudinov, A. L.; Bouldin, C. E.; Rehr, J. J.; Sims, J.; Hung, H. Parallel Calculation of Electron Multiple Scattering Using Lanczos Algorithms. *Phys. Rev. B: Condens. Matter Mater. Phys.* **2002**, *65* (10), 104107. (b) Ankudinov, A. L.; Ravel, B.; Rehr, J. J.; Conradson, S. D. Real-Space Multiple-Scattering Calculation and Interpretation of X-ray-Absorption Near-Edge Structure. *Phys. Rev. B: Condens. Matter Mater. Phys.* **1998**, *58* (12), 7565−7576.
(33) Neese, F. The ORCA program system. *WIRES Comput. Mol. Sci.* **2012**, *2* (1), 73−78.
(34) (a) Grimme, S.; Ehrlich, S.; Goerigk, L. Effect of the Damping Function in Dispersion Corrected Density Functional Theory. *J. Comput. Chem.* **2011**, *32* (7), 1456−1465. (b) Weigend, F.; Ahlrichs, R. Balanced Basis sets of Split Valence, Triple Zeta Valence and Quadruple Zeta Valence Quality for H to Rn: Design and Assessment of Accuracy. *Phys. Chem. Chem. Phys.* **2005**, *7* (18), 3297−3305.
(35) Becke, A. D. Density-Functional Exchange-Energy Approximation with Correct Asymptotic Behavior. *Phys. Rev. A: At., Mol., Opt. Phys.* **1988**, *38* (6), 3098−3100.
(36) Stoychev, G. L.; Auer, A. A.; Neese, F. Automatic Generation of Auxiliary Basis Sets. *J. Chem. Theory Comput.* **2017**, *13* (2), 554−562.
(37) Perdew, J. P.; Ernzerhof, M.; Burke, K. Rationale for Mixing Exact Exchange with Density Functional Approximations. *J. Chem. Phys.* **1996**, *105* (22), 9982−9985.
(38) (a) Adamo, C.; Barone, V. Toward Reliable Density Functional Methods Without Adjustable Parameters: The PBE0 model. *J. Chem. Phys.* **1999**, *110* (13), 6158−6170. (b) Neese, F.; Wennmohs, F.; Hansen, A. Efficient and Accurate Local Approximations to Coupled-Electron Pair Approaches: An Attempt to Revive the Pair Natural Orbital Method. *J. Chem. Phys.* **2009**, *130* (11), 114108. (c) Izsák, R.; Neese, F. An Overlap Fitted Chain of Spheres Exchange Method. *J. Chem. Phys.* **2011**, *135* (14), 144105.
(39) (a) Autschbach, J.; Ziegler, T. Nuclear Spin−Spin Coupling Constants from Regular Approximate Relativistic Density Functional Calculations. I. Formalism and Scalar Relativistic Results for Heavy Metal Compounds. *J. Chem. Phys.* **2000**, *113* (3), 936−947. (b) Autschbach, J.; Ziegler, T. Nuclear Spin−Spin Coupling Constants from Regular Approximate Relativistic Density Functional Calculations. II. Spin−Orbit Coupling Effects and Anisotropies. *J. Chem. Phys.* **2000**, *113* (21), 9410−9418. (c) Autschbach, J. Two-Component Relativistic Hybrid Density Functional Computations of Nuclear Spin-Spin Coupling Tensors Using Slater-Type Basis Sets and Density-Fitting Techniques. *J. Chem. Phys.* **2008**, *129* (9), 094105. (d) Autschbach, J. Erratum: Two-Component Relativistic Hybrid Density Functional Computations of Nuclear Spin-Spin Coupling Tensors Using Slater-Type Basis Sets and Density-Fitting Techniques J. Chem. Phys. 129, 094105 (2008)]. *J. Chem. Phys.* **2009**, *130* (20), 209901. (e) Autschbach, J. Magnitude of Finite-Nucleus-Size Effects in Relativistic Density Functional Computations of Indirect NMR Nuclear Spin−Spin Coupling Constants. *ChemPhysChem* **2009**, *10* (13), 2274−2283.
(40) (a) Maganas, D.; Roemelt, M.; Havecker, M.; Trunschke, A.; Knop-Gericke, A.; Schlogl, R.; Neese, F. First Principles Calculations of the Structure and V L-edge X-ray Absorption Spectra of V_2O_5 Using Local Pair Natural Orbital Coupled Cluster Theory and Spin-Orbit Coupled Configuration Interaction Approaches. *Phys. Chem. Chem. Phys.* **2013**, *15* (19), 7260−7276. (b) Roemelt, M.; Neese, F. Excited States of Large Open-Shell Molecules: An Efficient, General, and Spin-Adapted Approach Based on a Restricted Open-Shell Ground State Wave function. *J. Phys. Chem. A* **2013**, *117* (14), 3069−3083.
(41) Neese, F. A Spectroscopy Oriented Configuration Interaction Procedure. *J. Chem. Phys.* **2003**, *119* (18), 9428−9443.
(42) Sure, R.; Grimme, S. Corrected Small Basis Set Hartree-Fock Method for Large Systems. *J. Comput. Chem.* **2013**, *34* (19), 1672−1685.

DOI: 10.1021/acs.inorgchem.8b01000
Inorg. Chem. 2018, 57, 11382−11392